Strain-Tunable Spin Filtering and Valley Splitting Coexisting with Anomalous Hall Effect in 2D Half-Metallic VSe₂/VN Heterostructure: Toward a Unified Spintronic-Valleytronic Platform

Vivek Chowdhury^a, Ahmed Zubair^{a,*}

^aDepartment of Electrical and Electronic Engineering, Bangladesh University of Engineering and Technology, Dhaka, 1205, Bangladesh

ARTICLE INFO

Keywords:
Valleytronics
strain
Spin-Filtering
Valley Splitting
2D Half-Metallic VSe₂/VN
Anomalous Hall Effect
Unified Spintronic-Valleytronic Platform
2D TMD
Heterostructure

ABSTRACT

Rapid progress in valleytronics and spintronics is limited by the scarcity of two-dimensional materials that simultaneously provide robust valley splitting and strong spin selectivity. Here we showed that a van der Waals heterostructure (VSe₂/VN) built from hexagonal VSe₂ and hexagonal VN addressed this gap. Using first-principles density functional theory, phonon, ab initio molecular dynamics stability tests. Bader charge analysis, and Wannier-based Berry-curvature calculations, we demonstrated an energetically and dynamically stable heterostructure that exhibited interlayer charge transfer and a work function intermediate between the constituent monolayers. The electronic structure showed a small indirect PBE gap (108.9 meV), with HSE06 indicating a half-metallic tendency; a sizable conduction-band valley splitting ($\Delta C_{KK'} = 22.9$ meV for spin-up and $\Delta C_{KK'} = 61.3$ meV for spindown); and pronounced spin asymmetry, where the spin-down channel showed a wide semiconducting gap (0.64 eV) while the spin-up channel was nearly gapless. These features yielded a high zero-strain spin-filter efficiency P = 75.4%, tunable to 82.5% under +4% biaxial tensile strain. The heterostructure also supported non-zero, valley-contrasting Berry curvature, and a large anomalous Hall conductivity (peak $\sigma_{xy} = 568.33$ S/cm). Importantly, mean-field estimation placed the ferromagnetic Curie temperature near room temperature at zero strain (T_C = 284.04 K), while T_C decreased to 183.9 K at +4% strain, the magnetic order remained robust to cryogenic temperatures, providing a beneficial tuning knob to balance spin-filter performance with thermal stability in device-relevant regimes. These results identified VSe₂/VN as a practical, strain-tunable platform for integrated valleytronic, spintronic devices, and for exploring anomalous Hall and valley-dependent transport phenomena.

1 Introduction

The failure of Dennard scaling has stopped the amazing progress of Moore's law, where voltage no longer scales with feature size. This has pushed power densities to a power wall and made a lot of transistors stay inactive as dark silicon [1]. As wire delays, leakage, and heat dissipation dominate, further clock scaling yields diminishing returns and energy efficiency becomes the primary constraint for information processing [2]. Spintronics addresses these challenges by utilizing the electron's spin as an information carrier, facilitating nonvolatile, energy efficient state variables, and efficient charge-spin conversion, which are foundational to technologies ranging from magnetic tunnel junction (MTJ) based memory/logic to spin-orbit-torque devices [3, 4]. The MTJ is essentially the tunneling analog of the giant magnetoresistance (GMR) spin-valve, but with the non-magnetic metal spacer replaced by an insulator. In MgO (001) barrier, GMR has been exhibited both theoretically and experimentally [5, 6]. Half-metallic ferromagnets (HMFs) and spinfiltering 2D materials are also another domain of spintronics. Theoretically, HMFs provide 100% spin polarization near the Fermi level. Heusler alloys like Co₂MnSi, Co₂FeSi, Manganite perovskites like La_{0.7}Sr_{0.3}MnO₃ and CrO₂ are

ahmedzubair@eee.buet.ac.bd (A. Zubair)

ORCID(s): https://orcid.org/0009-0006-6180-8398 (V. Chowdhury); 0000-0002-1833-2244 (A. Zubair)

some classes of HMFs [7]. Spin-filtering uses the idea of ferromagnetic insulating barrier where electrons with spins aligned to the barrier's magnetization tunnel more readily than opposite spins. For example, ferrimagnetic CoFe₂O₄ barrier can be used as room-temperature spin-filtering device [6]. By using few-layer barriers and graphene contacts giant tunneling magnetoresistance (TMR) can be shown that grows with the number of CrI₃ layers [8].

In contrast, valleytronics leverages the momentum-space valley index and Berry curvature in 2D crystals to generate and control dissipationless transverse responses offering an orthogonal route to encode and manipulate information [9]. Identification of efficient valleytronic systems is essential to supersede modern charge or spin-based semiconductor devices [9]. By manipulating the valley degree of freedom, energy degeneracy can be broken in two unequal valleys, considering the strong spin-orbit coupling (SOC) [10]. Different methods have been introduced to enhance the valley degeneracy so far, including time reversal symmetry (TRS) violation [11] using magnetic doping [12], applied external magnetic field [13], magnetic proximity effects [14], and circularly polarized light pump [15]. Magnetic doping creates lattice distortion or impurity scattering, and the magnetic field can introduce only a small valley splitting of 0.1-0.2 meV/T [16]. Besides, circularly polarized light pumping is not suitable for valleytronic applications due to small carrier lifetime (~1ns) and lack of control [17]. Transition-metal dichalcogenides (TMDs) are proven to be very successful for the application of valleytronic, spintronic, optoelectronic

^{*}Corresponding author

vivekchybuet031@gmail.com (V. Chowdhury);

and biomedical devices [18, 19, 20, 21]. Moreover, they have the features of a tunable bandgap within the range of 1 to 2 eV induced by strong photoluminescence and large binding energy due to the excitonic effect [22]. Especially TMDs with H-phase have intrinsic broken spatial inversion symmetry (SIS), strong SOC, and large spin valley splitting at K/K' valley, which make them potential candidates for valleytronics [23, 24, 25].

The 2D magnetic substrate forming a van der Waals (vdW) heterostructure with 2D layered materials can eliminate impurity scattering, which makes it a good choice for fabricating valleytronic devices [26, 27]. The magnetic proximity effect enables monolayer MoTe₂ deposited on ferromagnetic substrate EuO a large valley splitting of 300 meV [28]. Experimental findings showed that valley splitting of monolayer WSe2 can be increased with the help of magnetic substrate EuS [29]. Heterostructure of WSe₂ and CrI₃ showed a considerable amount of valley splitting [30]. Besides, interfacial orbital hybridization allows a larger valley splitting in stanene/CrI₃ heterostructure [13]. Giant valley splitting (412 meV) was observed in 2D WS₂/h-VN heterostructure [31]. Valley splitting in the heterostructure of MoTe₂/MnS₂ can reach up to 55.3 meV [32]. At compressive strain, good valley splitting was reported in WSe₂/CrSnSe₃ [33]. For heterostructure MnPSe₃/WSe₂, more than 30 meV valley splitting was found [34]. MoTe₂/WTe₂ showed giant valley splitting in a recent report [35]. VX_2 (X = S, Se, Te) emerged as a member of ferrovalley materials [36], where interaction of d electrons induced spontaneous valley splitting due to broken TRS and SIS.

Monolayer hexagonal VTe2, VS2, and VSe2 are basic examples of ferrovalley materials. Room-temperature ferromagnetism was observed in ultrathin 3 nm VTe2 grown by chemical vapor deposition (CVD), which provides its usefulness in valley polarization [37]. Due to strong SOC effect and magnetism, giant valley splitting is observed in VTe₂ [38, 39]. Additionally, it can be used in spin-calorimetry applications due to its higher spin polarizability [39]. VSe₂ is useful for room temperature because of its high Curie temperature (up to 590 K) [40]. Recently, the synthesis of VSe₂ has encouraged researchers to use its potential as a magnetic and valleytronic material [41, 36]. It has both intrinsic valley splitting, ferromagnetism [41], and possesses T and H phases [42]. The h-VN, which also has a large Curie temperature of 768 K, can be used as a ferromagnetic halfmetallic substrate for forming heterostructures [43].

Spin-filtering and valleytronic properties in related systems have been explored in previous reports. For instance, 25% W-doped monolayer VSe₂ (with SOC) was reported to filter spin-down electrons with an energy gap of 0.8 eV [19]. Similarly, the 2H-VS₂/h-VN heterostructure exhibited straininduced valley splitting, although with a relatively limited tunability [26]. Furthermore, the anomalous Hall conductivity (AHC) values obtained in several previous works [31] remain comparatively modest, leaving room for improvement in high-performance valleytronic and spintronic device applications.

Previous studies have examined spin-filtering and valleytronic behavior separately, but a combined realization in a single material has not yet been reported. Motivated by this gap, we systematically explored multiple stacking configurations of the previously unexamined VSe₂/VN heterostructure by varying the interlayer distance. We investigated the system's stability using formation energy, phonon dispersion, and molecular dynamics simulations. After identifying the optimized heterostructure, we analyzed its electronic, magnetic, and structural properties, including band structure, density of states, magnetization easy axis, and Bader charge analysis using DFT calculations. Finally, by applying both compressive and tensile strain, we demonstrated a strain-tunable spin-filtering response together with giant valley splitting and AHC, unlocking the ability of this system for future spintronic and valleytronic device applications.

2 Computational Details

First-principles calculations of structural and electronic properties were performed using DFT-based tool Quantum ESPRESSO [44]. The Perdew-Burke-Ernzerhof (PBE) functional was used for generalized gradient approximation (GGA) of exchange-correlation energy. Fully relativistic projector augmented wave (PAW) pseudopotentials of V, Se, and N were used to account for the effect of SOC. The DFT-D3 method was used for van der Waals correction. The plane-wave kinetic energy cutoff was selected as 680 eV for expanding the wave functions, and the cutoff was selected as 6800 eV for charge density and potentials. Structural relaxation was performed until forces on atoms had converged down to 10^{-2} eV/Å and total energy converged below the threshold of 10^{-6} eV/Å. Due to the strong repulsion of localized d electrons, the GGA+U method was used with U = 2.00 eV and J = 0.87 eV for the 3d orbitals of V [36]. A Gamma-centered Monkhorst-Pack scheme with a k-point mesh of $(8\times8\times1)$ and $(12\times12\times1)$ was used for the relaxation and self-consistent field (SCF) calculations, respectively. To obtain the density of states (DOS) and the projected density of states (PDOS), a k-grid of $(32 \times 32 \times 1)$ was used in non-self-consistent field (NSCF) calculations. To estimate the accurate band structure the Heyd-Scuseria-Ernzerhof (HSE06) was used.

E-k diagrams were constructed along the path M \rightarrow K \rightarrow Γ \rightarrow K' \rightarrow M of the first Brillouin zone, with 35 k-points between each high-symmetry point. To avoid interactions between adjacent layers, a vacuum layer with a thickness of 20 Å was added. The valley splitting was defined as $\Delta C_{KK'}$ for the conduction band (CB) and $\Delta V_{KK'}$ for the valence band (VB), where both $\Delta C_{KK'}$ and $\Delta V_{KK'}$ are given by $E_K - E_{K'}$. Here, E_K and $E_{K'}$ denote the energy (top of the VB and bottom of the CB) at the K and K' points of the Brillouin zone, respectively.

Moreover, projected band structures were calculated to show the contribution of orbitals of a particular atom in the band structure. Biaxial strain (ε) was calculated using $\varepsilon=\frac{a-a_0}{a_0}$, where a is the strained lattice constant and a_0

is the equilibrium lattice constant. Spin projection on band structure was shown using a color map by varying the spin operator from -0.50 to 0.50.

To observe the dynamic stability of the heterostructure, the Phonopy package [45] was used. Here, the dimension of the supercell was taken as $(4 \times 4 \times 1)$ and a large value of kinetic energy cutoff (950 eV) was used. To avoid flexural phonons near Γ point, the structure was assumed to be isolated as 2D. To plot the phonon bands, $\Gamma \to M \to K \to \Gamma$ path was selected with 100 band points. The *ab initio* molecular dynamics (AIMD) simulations were performed in the canonical (NVT) ensemble using the Nosé–Hoover thermostat for 5 ps to assess the thermal stability of the system. For energetic stability, the formation energy was calculated for different stackings of the heterostructure by,

$$E_{\text{formation}} = E_{\text{VSe}_{2}/\text{VN}} - E_{\text{VSe}_{2}} - E_{\text{VN}}$$
 (1)

Charge density difference (CDD) was calculated using the formula,

$$\Delta \rho(\mathbf{r}) = \rho_{\text{VSe}_2/\text{VN}}(\mathbf{r}) - \rho_{\text{VSe}_2}(\mathbf{r}) - \rho_{\text{VN}}(\mathbf{r})$$
 (2)

where $\rho_{\rm VSe_2/VN}({\bf r})$ is the charge density of the full heterostructure, $\rho_{\rm VSe_2}({\bf r})$ is the charge density of the isolated VSe₂ monolayer (in the same atomic positions as in the heterostructure), and $\rho_{\rm VN}({\bf r})$ is the charge density of the isolated VN monolayer (in the same atomic positions as in the heterostructure). Here, ${\bf r}$ denotes the space vector. Bader charge analysis was conducted using the code by Henkelman group [46]. Work function was calculated using the formula,

$$\phi = E_{\text{vacuum}} - E_{\text{F}} \tag{3}$$

where E_{vacuum} is the vacuum energy level and E_F is the Fermi level. Spin density was calculated using:

$$\Delta \rho_{\rm S}(\mathbf{r}) = \rho_{\uparrow}(\mathbf{r}) - \rho_{\downarrow}(\mathbf{r}) \tag{4}$$

Here, $\rho_{\uparrow}(\mathbf{r})$ denotes the positive spin density and $\rho_{\downarrow}(\mathbf{r})$ denotes the negative spin density.

To calculate Berry curvature and anomalous Hall conductivity, the maximally localized Wannier functions (MLWF) were constructed using Wannier90 [47] with 60 Wannier functions generated from 60 Bloch bands spanning the relevant energy window. Projections included the s, p and d orbitals of V atoms and s and p orbitals of Se and N atoms. The initial Wannierization was performed on a Monkhorst–Pack ($12 \times 12 \times 1$) k-point grid, from which the real-space Hamiltonian and tight-binding model were obtained. Berry curvature calculations were carried out using the Wannier90 post-processing tool with respect to the path $M \to K \to \Gamma \to K' \to M$. The AHC was computed using the Berry curvature on an interpolated k-point mesh of ($100 \times 100 \times 100$).

Table 1Structural, electronic, and magnetic properties of pristine VSe₂ and VN monolayers

Property	VSe ₂	VN
Lattice parameter (Å)	3.347	3.224
Bond length (Å)	2.50	1.86
Bond angle	79.3 °	120 °
Magnetization ($\mu_{ m B}$ per unit cell)	1.00	1.98
Work function (eV)	5.47	3.81

3 Results and Discussion

3.1 Pristine Hexagonal VSe₂ and VN Monolayer

The structural model, electronic band structure, and PDOS of the pristine hexagonal VSe₂ monolayer are shown in Figs. 1(a-e). The side and top views appear in Figs. 1(a) and (b), respectively. The unit cell of this 2D magnetic semiconductor comprised three atoms: one V and two Se; and as summarized in Table 1, was characterized by a lattice parameter of 3.347 Å, a V-Se bond length of 2.50 Å, an induced magnetization of 1.00 μ_B per unit cell and a Se-V-Se bond angle of 79.3°. These structural parameters were consistent with values reported in the literature [19]. Fig. 1(c) displays the spin-polarized band structure (without SOC) of monolayer VSe₂, where the valence band maximum (VBM) occurred at K^{\prime} and the conduction band minimum (CBM) occurred at M, revealing an indirect band gap. Figs. S1(a) and (b) show the spin-polarized band structure (with SOC) together with the work function. We found that the valley splitting $\Delta V_{KK'}$, bandgap, and work function were 79.2 meV, 0.29 eV and 5.47 eV respectively, in agreement with previous studies [40, 48].

The PDOS analysis, shown in Figs. 1(d) and (e), highlights the contributions of different atomic orbitals to the electronic structure of VSe₂. Fig. 1(d) presented the orbital PDOS for V: s, V: p, V: d states, and the V:d orbitals dominated near the Fermi level (E_F). At the CBM of VSe₂, the contributions primarily arose from V: d orbitals; especially d_{z^2} , d_{zx} , and d_{xy} in the spin-down channel. In contrast, the VBM of VSe₂ was contributed by V: d orbitals, mainly d_{z^2} and d_{zx} , in the spin-up channel. Fig. 1(e) shows the PDOS from Se: s and Se: p orbitals. At both VBM and CBM, Se contributions were very minor. By contrast, Se exhibited larger contributions than V in the lower valence bands for both spin channels; most notably Se: p_z , Se: p_x , and Se: p_y in the spin-down channel and Se: p_z , Se: p_y in the spin-up channel

Figs. 1(f-j) present the structural models, electronic band structures, and projected density of states (PDOS) for a pristine hexagonal VN monolayer. The side and top views are shown in Figs. 1(f) and (g). As referred (Table 1), we calculated the values of lattice parameter, bond length, bond angle, and induced magnetization after optimization, which were 3.224 Å, 1.86 Å, 120° , and $1.98 \mu_{\text{B}}$ per unit

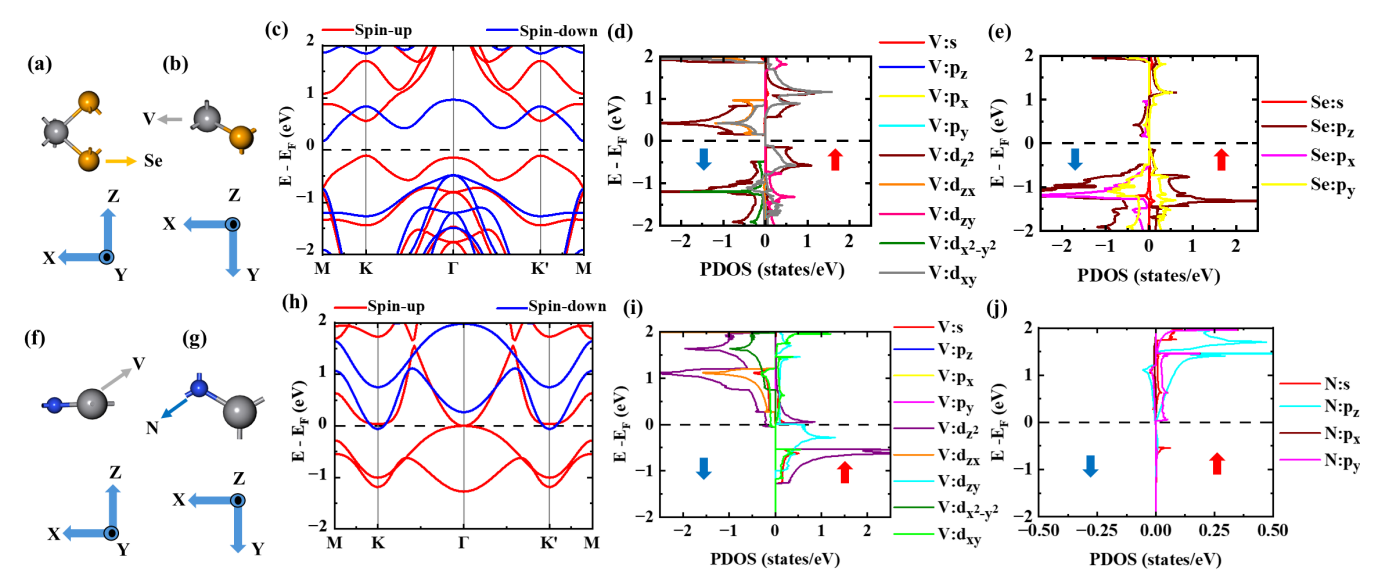


Figure 1: (a) Side view of pristine hexagonal VSe₂ monolayer. (b) Top view of pristine hexagonal VSe₂ monolayer. (c) Spin-polarized band structure (without SOC) of pristine hexagonal VSe₂ monolayer. (d) PDOS of s, p and d orbitals of the V atom. (e) PDOS of s, p orbitals of the Se atom. (f) Side view of pristine hexagonal VN monolayer. (g) Top view of pristine hexagonal VN monolayer. (h) Spin-polarized band structure (without SOC) of pristine hexagonal VN monolayer. (i) PDOS of s, p and d orbitals of the V atom. (j) PDOS of s, p orbitals of the N atom. The red line and red arrow represent the spin-up channel, while the blue line and blue arrow represent the spin-down channel.

cell, respectively. The spin-polarized band structure (without SOC) in Fig. 1(h) revealed a half-metallic ground state, while the corresponding calculation (with SOC) was provided in Fig. S2(a). These results are consistent with previous reports [49]. We determined the work function of the hexagonal VN monolayer to be 3.81 eV (Fig. S2(b)), which is also in close agreement with earlier findings [26].

The orbital-resolved PDOS of V and N atoms are displayed in Figs. 1(i) and (j). The PDOS was dominated by the V atom in the pristine hexagonal VN monolayer. The N atom contributed less to the PDOS, consistent with reduced orbital overlap associated with its smaller size. Among the N orbitals, the p_z orbital in the spin-up channel contributed the most, although it remained much smaller than the V contribution; in the spin-down channel, the N contribution was negligible. By contrast, the V atom exhibited prominent weight in both spin channels. A notable feature is that the spin-down channel showed no states below E_F ; near and above E_F , V: d_{z^2} and V: d_{zx} contributed strongly, with a smaller contribution from V: d_{xy} . In the spin-up channel, finite weight appeared both below and above E_F , with V: d_{z^2} and V: d_{zy} providing the largest contributions.

3.2 Structural and Stability Analysis of VSe_2/VN Heterostructure

Both VSe_2 and VN monolayers have been synthesized experimentally. Prior studies [50, 51] demonstrate that VSe_2 can be grown epitaxially by molecular beam epitaxy (MBE) and by chemical vapor deposition (CVD). Thin VN films have also been realized using unfiltered cathodic arc evaporation (CAE) [52]. In addition, *ab initio* calculations support

the dynamical stability of these monolayers [19, 49]. As summarized in Table 1, we evaluated the lattice mismatch between VSe_2 and VN monolayers was 3.82%, which is below the commonly used 5% compatibility threshold [53], making this pair a promising candidate for heterostructure fabrication.

Fig. 2 illustrates the various stacking patterns in the VSe_2/VN heterostructure. The top row displays top views of six configurations and the bottom row shows side views with the corresponding interlayer distance (D). Configurations 1, 2, 5, and 6 followed an AA stacking, whereas configurations 3 and 4 adopted AB stacking. From Table 2, we determined that only stackings 1 and 2 had negative formation energies; the others were energetically unfavorable. Among these, stacking 2 emerged as the most stable, with a formation energy of -0.95 eV per unit cell and an in-plane lattice parameter of 3.328 Å per unit cell. This level of stabilization is comparable to that reported for other 2D van der Waals heterostructures, such as MoS_2/ZnO [54].

To assess the dynamical and thermal stability of VSe₂/VN, we computed the phonon dispersion and performed AIMD, as shown in Figs. 3(a) and (b). In Fig. 3(a), the phonon spectrum contains 15 branches; three times the number of atoms in the unit cell (five) as expected. The absence of imaginary frequencies ensured the system's dynamical stability. Figure 3(b) presents the total energy evolution at 373 K over 5 ps using the NVT ensemble. The only minor fluctuations observed in the total energy indicate that the VSe₂/VN heterostructure is thermally stable under these conditions.

Fig. 3(c) shows the optimized structural parameters of the VSe₂/VN heterostructure. As depicted in Table 3, We

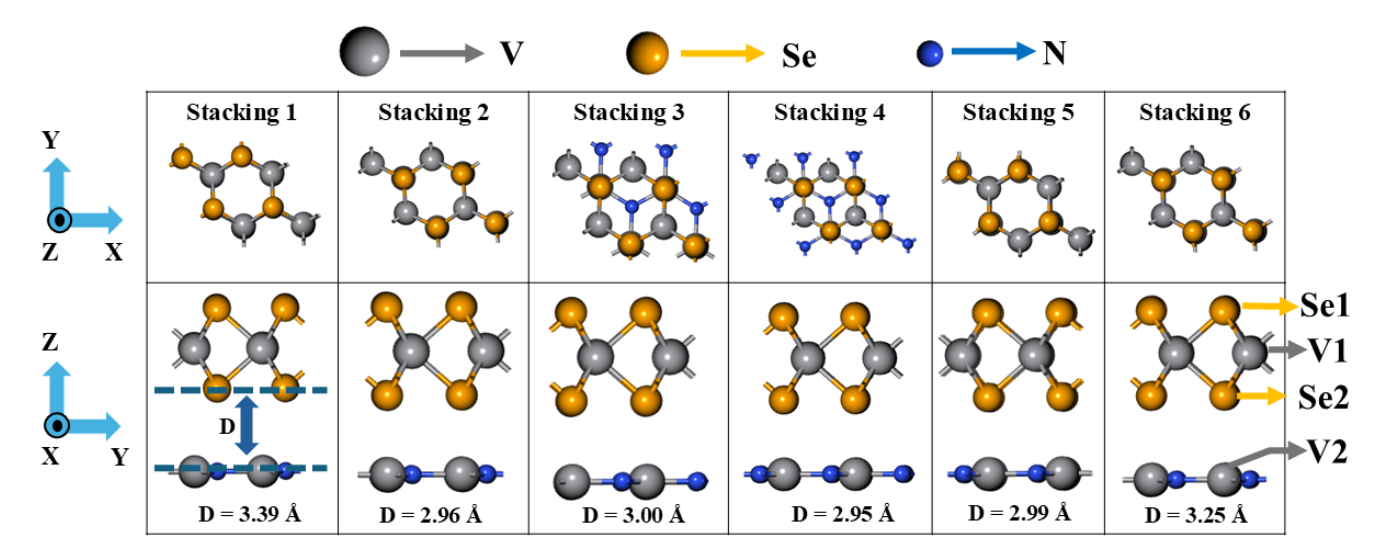


Figure 2: Different stackings of VSe_2/VN ($2 \times 2 \times 1$ supercell) heterostructure. First row indicates the top views and second row indicates the side views of the heterostructure with varying interlayer distance (D).

Table 2Structural properties and formation energies for the six stacking configurations

Stacking	Interlayer distance (Å)	Lattice parameter (Å / unit cell)	Formation energy (eV / unit cell)
Stacking 1	3.39	3.230	-0.53
Stacking 2	2.96	3.328	-0.95
Stacking 3	3.00	3.256	0.26
Stacking 4	2.95	3.257	0.21
Stacking 5	2.99	3.251	0.22
Stacking 6	3.25	3.250	0.41

Table 3Optimized structural, electronic, and magnetic properties of the VSe₂/VN heterostructure

Property	Value
Lattice parameter (Å)	3.328
Bond angle	Se-V-Se: 79.29 °
	V–N–V $/$ N–V–N: 120 $^{\circ}$
Bond length (Å)	V-Se: 2.51
	V-N: 1.87
Magnetization ($\mu_{ m B}$ per unit cell)	3.00
Work function (eV)	4.53
Interlayer distance (Å)	2.96

found the unit cell lattice parameter, Se–V–Se and V–N–V/N–V–N bond angles to be 3.328 Å, 79.29°, and 120°, respectively. We determined the V–Se bond length to be 2.51 Å and the V–N bond length to be 1.87 Å. The total magnetization was found to be 3.00 $\mu_{\rm B}$ per unit cell. We evaluated the work function of the VSe₂/VN heterostructure to be 4.53 eV (Fig. 3(d)), obtained from the difference between the vacuum level and the Fermi level. The interlayer

Table 4

Bader charge analysis (in e) for isolated monolayers and the heterostructure and the resulting net charge transfer, ΔN (heterostructure – isolated). Negative ΔN indicates electron gain and positive ΔN indicates electron loss

Element	Isolated layer	Heterostructure	ΔN
V1	+1.18	+1.15	-0.03
Se1	-0.59	-0.59	0.00
Se2	-0.59	-0.67	-0.08
V2	+1.49	+1.52	+0.03
N	-1.49	-1.41	+0.08

distance between the monolayers was 2.96 $\mbox{\normalfont\AA}$, as mentioned for stacking 2.

3.3 Electronic Property of VSe₂/VN Heterostructure

We employed Bader charge analysis to quantify the net charge transfer for each atom in the VSe_2/VN heterostructure. In this approach, the atomic charge Q_i was evaluated from the Bader electron count and the valence reference using the formula below:

$$Q_i \equiv Z_i^{\text{val}} - q_i^{\text{B}} \tag{5}$$

where Q_i is the net atomic charge on atom i, Z_i^{val} is its valence electron count and q_i^{B} is the Bader charge obtained from the charge density analysis.

In Table 4, we computed Q_i for V1 (V atom in VSe₂), V2 (V atom in VN), Se1 (Se atom far from VN), Se2 (Se atom close to VN), and the N atom for both the isolated monolayers and the heterostructure, and then evaluated the net charge

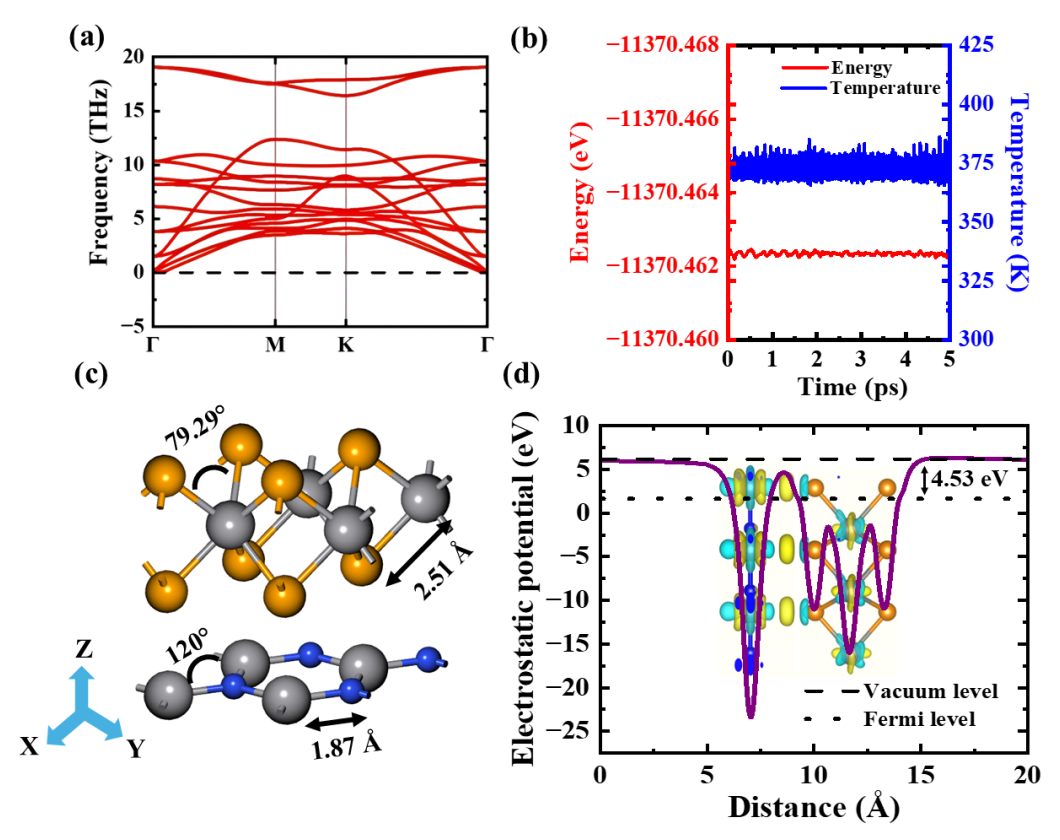


Figure 3: (a) Phonon dispersion diagram of the VSe $_2$ /VN heterostructure showing the absence of any imaginary frequencies, confirming its dynamic stability. (b) Variation of total energy and temperature of the VSe $_2$ /VN heterostructure under the NVT ensemble at 373 K, recorded from 0 to 5 ps with a timestep of 1 fs. (c) Optimized atomic structure of the VSe $_2$ /VN heterostructure. (d) Work function along with CDD diagram (with isosurface value of 0.0033 eV^{-3}) of the VSe $_2$ /VN heterostructure with respect to z-axis, where the dashed line represents the vacuum level and the dotted line denotes the Fermi level. Cyan and yellow represent electron depletion and accumulation, respectively.

transfer, ΔN (heterostructure – isolated). For isolated VSe₂, the V atom showed electron loss (+1.18 e) and each Se atom showed electron accumulation (-0.59 e). In isolated VN, the V atom likewise exhibited electron loss (+1.49 e), larger than for V1, while the N atom exhibited electron accumulation (-1.49 e), maintaining charge neutrality.

After forming the heterostructure, charge redistributed and the individual monolayers were no longer neutral. The calculated ΔN values indicated electron gain for V1 (-0.03 e) and Se2 (-0.08 e), electron depletion for V2 (+0.03 e) and N (+0.08 e), and essentially no net transfer for Se1 (0.00 e). We therefore concluded that electrons depleted from the VN layer and accumulated on the VSe₂ layer upon heterostructure formation.

This conclusion was supported by the CDD diagram and the work function analysis in Fig. 3(d). The CDD showed electron accumulation near the VSe₂ layer and depletion near the VN layer, with no change at Se1. Consistently, the work functions of VSe₂, VN, and the VSe₂/VN heterostructure were 5.47 eV, 3.81 eV, and 4.53 eV, respectively (Tables 1 and 3). Because electrons flow from the lower to the higher work function until the Fermi levels are aligned, charge was transferred from VN to VSe₂, stabilizing the heterostructure at a work function of 4.53 eV.

We considered SOC in all band structure calculations to expose valley splitting. For a 2D single layer with two inequivalent valleys labeled by $\tau = \pm 1$ (for K and K'), a two-band $k \cdot p$ basis $\{|c\rangle, |v\rangle\}$ near each valley can be defined where Pauli matrices $\sigma_{x,y,z}$ act in the (c,v) subspace and a spin index $s = \pm 1$ denotes \uparrow, \downarrow . The spinless Dirac-type block can be defined [23]:

$$H_0(\mathbf{k}, \tau) = \hbar v \left(\tau k_x \sigma_x + k_y \sigma_y \right) + \frac{\Delta}{2} \sigma_z \tag{6}$$

Here, v is the effective Dirac velocity, Δ is the spinless band gap. SOC at the band edges is captured by valley and spin-dependent shifts that projects onto the conduction and valence sectors:

$$H_{\text{SOC}}(\tau, s) = \tau s \left(\lambda_c \Pi_c + \lambda_v \Pi_v \right), \qquad \Pi_{c/v} = \frac{\sigma_0 \pm \sigma_z}{2} \tag{7}$$

where σ_0 is the identity in band space, $\Pi_{c/v}$ projects onto the conduction/valence edges, $\tau=\pm 1$ labels the valleys, $s=\pm 1$ labels the out-of-plane spin, and $\lambda_{c/v}$ are the SOC coupling strengths at the conduction/valence edges. At the band extrema ($\mathbf{k}=0$), $H_0+H_{\rm SOC}$ is diagonal, yielding

$$E_{\rm c}(\tau,s) = +\frac{\Delta}{2} + \tau s \,\lambda_c, \qquad E_{\rm v}(\tau,s) = -\frac{\Delta}{2} - \tau s \,\lambda_v \ \ (8)$$

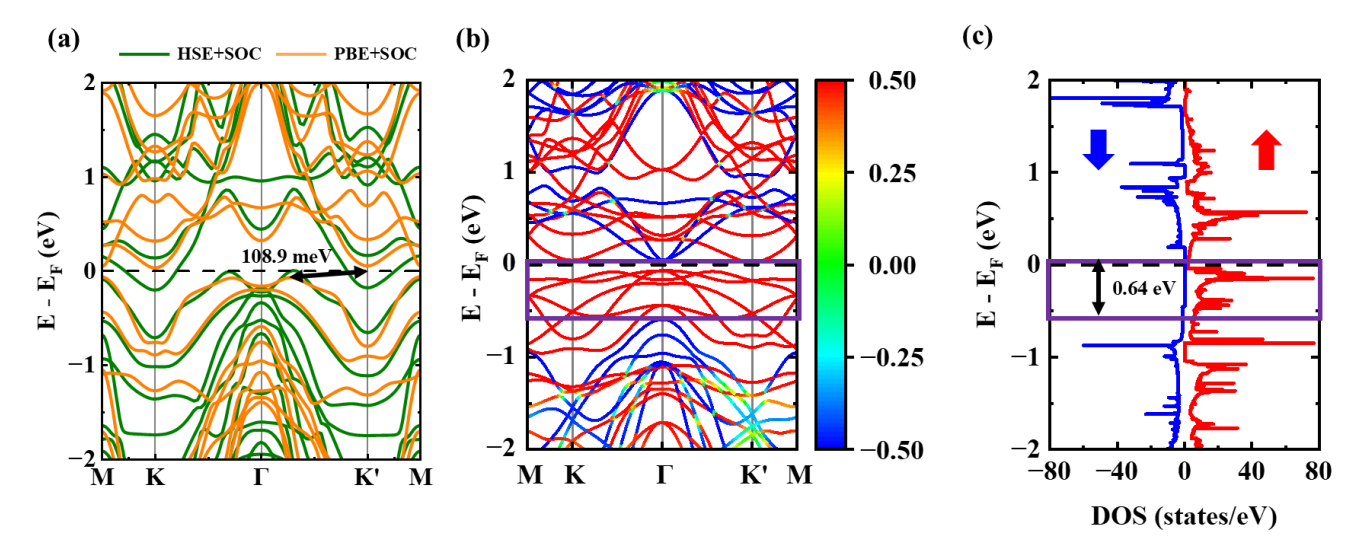


Figure 4: (a) Band structure (with SOC) of unit cell VSe $_2$ /VN heterostructure. Green line indicates band structure with HSE06 functional and orange line indicates band structure with PBE functional. (b) Band structure (with SOC) ($2 \times 2 \times 1$ supercell) of VSe $_2$ /VN heterostructure. The color map indicates expectation values of the spin operator on the spinor wave-functions ranging from -0.50 (blue) to +0.50 (red). (c) Spin-polarized DOS ($2 \times 2 \times 1$ supercell) of VSe $_2$ /VN heterostructure. Blue arrow, red arrow indicate spin-down channel and spin-up channel, respectively. The purple box shows the forbidden energy window (0.64 eV) of spin-down channel in (b) and (c).

Fixing the spin s, the valley splittings (energy differences between K and K') are

$$\Delta C_{KK'} = E_c(+1, s) - E_c(-1, s) = 2\lambda_c s \tag{9}$$

$$\Delta V_{KK'} = E_v(+1, s) - E_v(-1, s) = 2\lambda_v s \tag{10}$$

Thus, SOC introduces valley splitting, which is also applicable for 2D heterostructures.

Figs. 4(a-c) represent the band structure and DOS of the VSe₂/VN heterostructure. In Fig. 4(a), the band structures (including SOC) are obtained using the PBE and HSE06 functionals. A small indirect band gap of 108.9 meV was found, extending from K' to a k-point between Γ and K', using the PBE functional, whereas the HSE06 functional resulted in a half-metallic nature of the heterostructure. The conduction band valley splitting was found to be more dominant. Using PBE and HSE06, $\Delta C_{KK'}$ was found to be 22.9 meV and 23.7 meV in the unit cell, respectively. As HSE06 is computationally expensive and the valley splittings were close for PBE and HSE06, further calculations were performed using the PBE functional. We calculated the PBE spin-polarized band structure $(2 \times 2 \times 1 \text{ supercell})$ of the heterostructure to account for the band-folding effect, as shown in Fig. 4(b). It was found that the spin-down channel showed a semiconducting gap (0.64 eV), whereas the spinup channel was nearly gapless (approximately 108.9 meV), consistent with the PBE result for the unit cell. The spinpolarized DOS of this supercell was also found to be consistent with the corresponding band structure; the spin-down channel exhibited a gap, whereas the spin-up channel was

nearly gapless, giving the system a half-metallic (close to spin-gapless) character.

This idea can be used to form a spin-filtering device, as mentioned in the study [19]. As illustrated in Fig. 5, the 0.64 eV energy window provides sufficient available states for the spin-up channel, whereas no states are present for the spin-down channel. Therefore, within this window, by applying external perturbation, spin-up electrons can be selectively transmitted and filtered out at the right contact.

In Figs. 6(a-d), the orbital projected band structure of VSe_2/VN are shown. In Fig. 6(a), V1:d contributed most strongly above E_F , whereas in Fig. 6(b) V2:d exhibited the larger weight below E_F . The V:s and V:p orbitals contributed negligibly. In contrast, as shown in Fig. 6(c), Se:p carried noticeable weight at lower-lying (deeper) energies but contributed negligibly near E_F . The N:p contribution was comparatively weak, consistent with the smaller size of the N atom (Fig. 6(d)). Similar to V, the Se:s and N:s orbitals contributed negligibly across the energy range.

Figs. S4(a-d) illustrate the PDOS (without SOC) to provide a clearer picture of the orbital contributions. Table 5 summarizes the orbital-decomposed weights for VSe₂/VN. Near E_F in the spin-up channel, the spectrum was dominated by V2: d_{z^2} (42.37%) and Se: p_z (25.44%), with additional weight from V1: d_{z^2} (17.11%), V2: d_{xy} (10.01%), and a minor Se: p_y component (5.07%); Se: p_x was negligible. For the spin-down channel at the CBM, the character was V: d dominated, led by V1: d_{z^2} (51.70%) with sizable V1: d_{zx} (19.58%), and V1: d_{xy} (14.03%), while Se: p_x and Se: p_z contributed only modestly (6.69% and 8.00%, respectively); V2-derived contributions were absent at the CBM and VBM. In contrast, at the VBM (spin-down) the weight redistributed

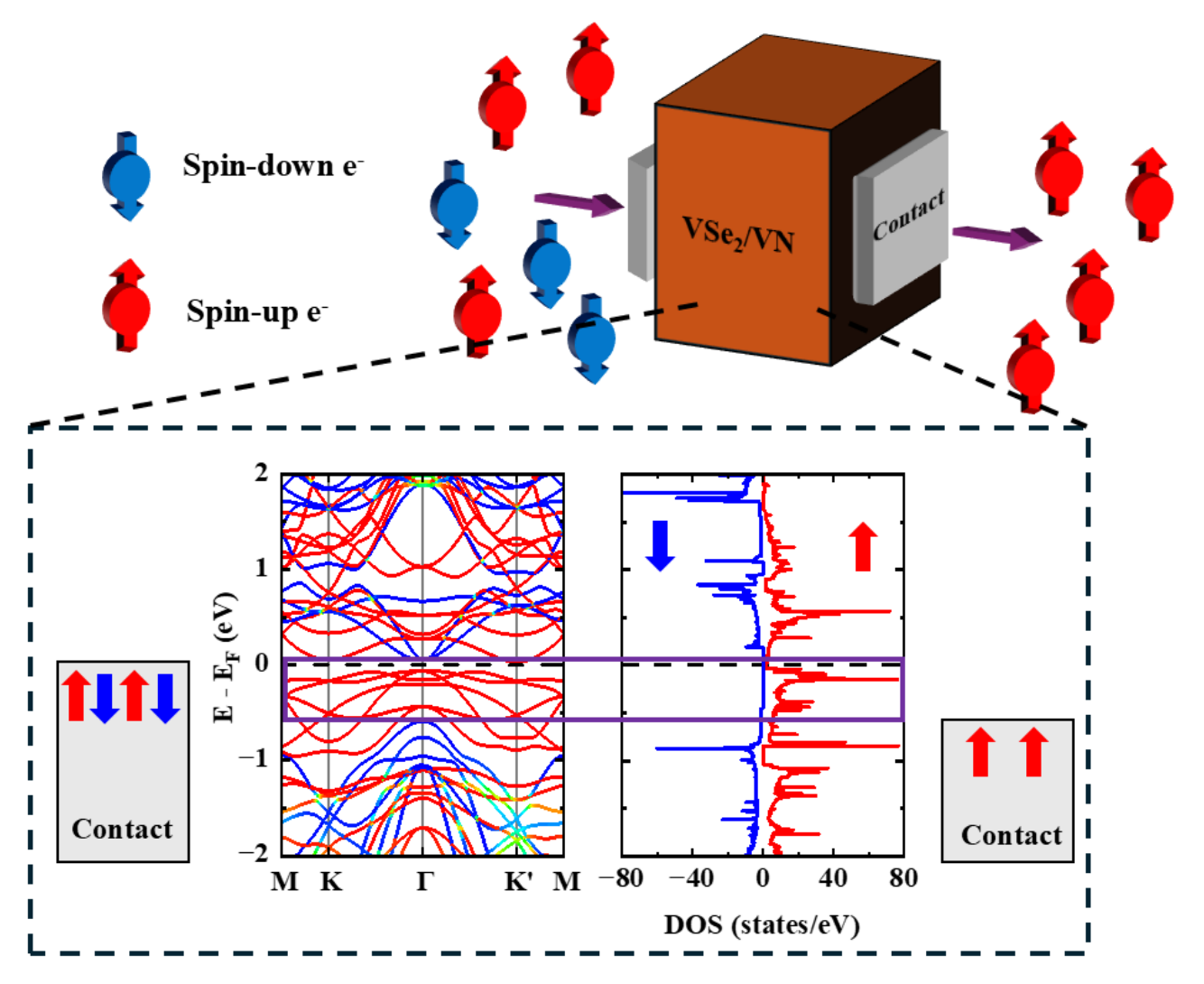


Figure 5: Schematic of a spin-filter using the VSe_2/VN ($2 \times 2 \times 1$ supercell) heterostructure. By applying external perturbation, spin-up electrons will be available for a certain energy window at the right contact.

 $\begin{tabular}{ll} \textbf{Table 5} \\ \textbf{Orbital contributions for VSe}_2/VN. \begin{tabular}{ll} \textbf{Entries are percentages for the spin-up channel near E_F and for the spin-down channel at the CBM and VBM \\ \end{tabular}$

	$V1: d_{z^2}$	$V1: d_{zx}$	$V1: d_{xy}$	$V1: d_{x^2-y^2}$	$V2: d_{z^2}$	$V2: d_{xy}$	Se: p_x	Se: p_y	Se: p_z
Spin-up channel near E_F	17.11%	_	_	_	42.37%	10.01%	_	5.07%	25.44%
Spin-down channel at CBM	51.70%	19.58%	14.03%	_	_	_	6.69%	_	8.00%
Spin-down channel at VBM	39.27%	_	_	19.82%	_	_	_	13.44%	27.47%

toward a mixed V–Se character: V1: d_{z^2} (39.27%) remained significant, Se: p_z (27.47%), Se: p_y (13.44%) became prominent and V1: $d_{x^2-y^2}$ (19.82%) emerged, whereas V1: d_{zx} and V1: d_{xy} were absent. The orbitals of N atom showed negligible contributions in all cases.

3.4 Magnetic Property of VSe₂/VN Heterostructure

We found the total magnetization of VSe₂/VN to be 3.00 $\mu_{\rm B}$ per unit cell. The magnetocrystalline anisotropy

energy (MAE) was calculated using the formula,

$$MAE = E_{\parallel} - E_{\perp} \tag{11}$$

where E_{\parallel} is the total energy with the magnetization constrained in-plane (parallel to the layer) and E_{\perp} is the total energy with the magnetization constrained out-of-plane (perpendicular to the layer). With this sign convention, MAE > 0 indicates a perpendicular (out-of-plane) easy axis, while MAE < 0 indicates an in-plane easy axis.

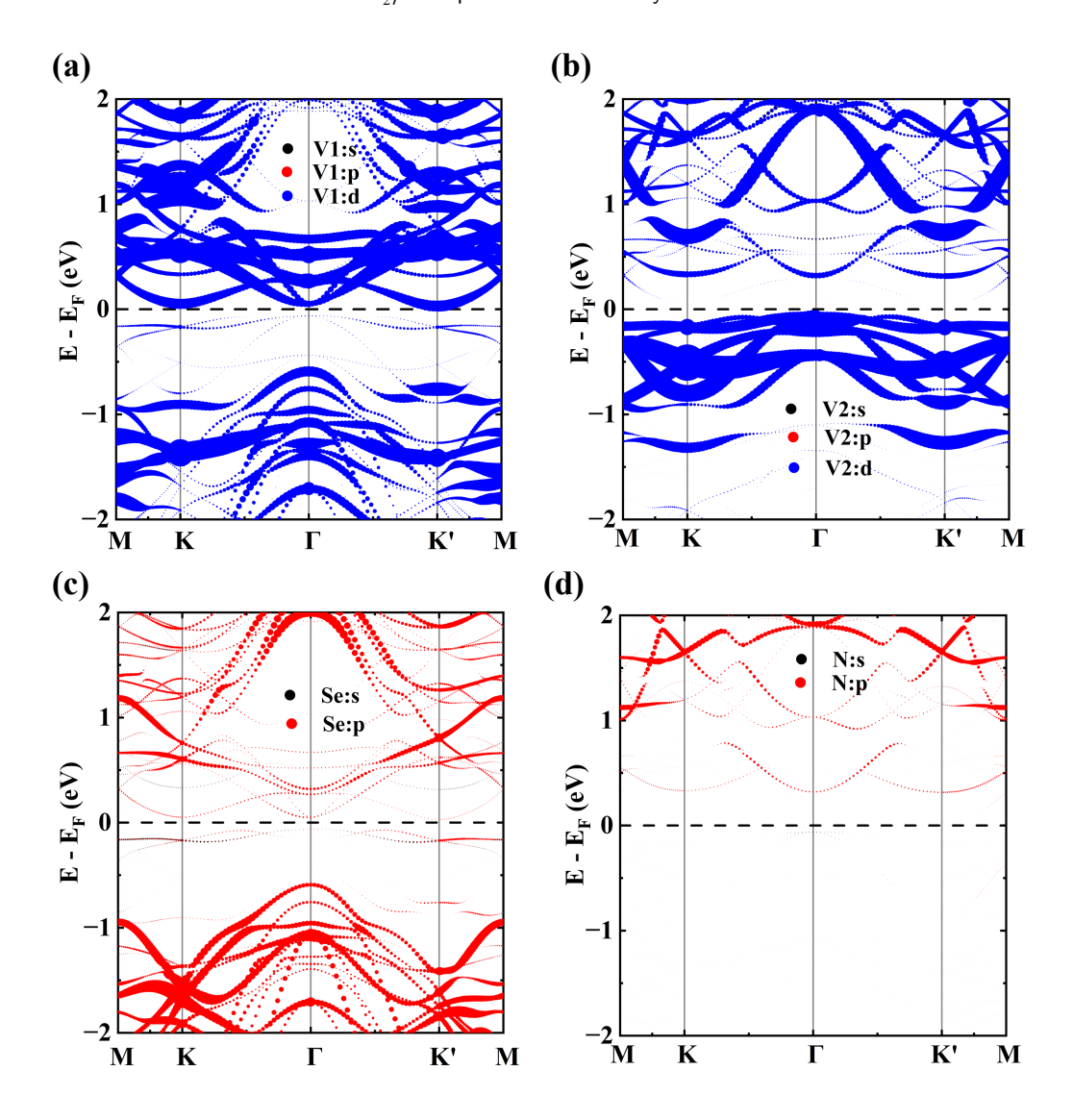


Figure 6: Orbital projected band structure of VSe_2/VN ($2 \times 2 \times 1$ supercell). (a) Projection of s, p, d orbitals of V1 (V atom of VSe_2). (b) Projection of s, p, d orbitals of V2 (V atom of VN). (c) Projection of s, p orbitals of Se. (d) Projection of s, p orbitals of N.

For the unstrained case, the MAE was +0.93 meV, indicating an out-of-plane easy axis. Under compressive (-4%) and tensile (+4%) strain, the MAE values were -1.279 and +1.247 meV, respectively. Thus, compressive strain favors an in-plane easy axis, whereas both the unstrained and tensile cases favor an out-of-plane easy axis. The tensile case further strengthens the out-of-plane preference compared with 0% strain.

We determined Curie temperature, T_C using mean field estimation as mentioned in the study [55].

$$T_{\rm C} = \frac{2(E_{\rm AFM} - E_{\rm FM})}{3k_{\scriptscriptstyle R}} \tag{12}$$

where k_B is the Boltzmann constant, E_{AFM} and E_{FM} are the total energies of the antiferromagnetic and ferromagnetic states per magnetic atom, respectively. The Curie temperature (T_C) of VSe_2/VN was found to be 284.04 K, which is

very close to room temperature (298 K). This indicates that the ferromagnetic order in VSe_2/VN should be thermally stable under ordinary laboratory conditions, making the system promising for room temperature spintronic applications. At compressive (-4%) and tensile (+4%) strain, the values of T_C were found to be 47.5 K and 183.9 K, respectively, highlighting the strong strain sensitivity of the magnetic ordering and suggesting that near-ambient operation is most favorable close to the unstrained state.

Figs. S3(a–e) illustrate the spin density, $\Delta \rho_s(\mathbf{r})$, under different strain conditions. Negative spin density was marked in cyan and positive spin density was marked in yellow. In the compressive strain regime (-2% and -1%), the negative spin density was weakened, whereas in the unstrained case and in the tensile regime (+1% and +2%), the negative spin density strengthened and then saturated. At tensile strain, the structure was found to have constant $\Delta \rho_s$. As a result, the

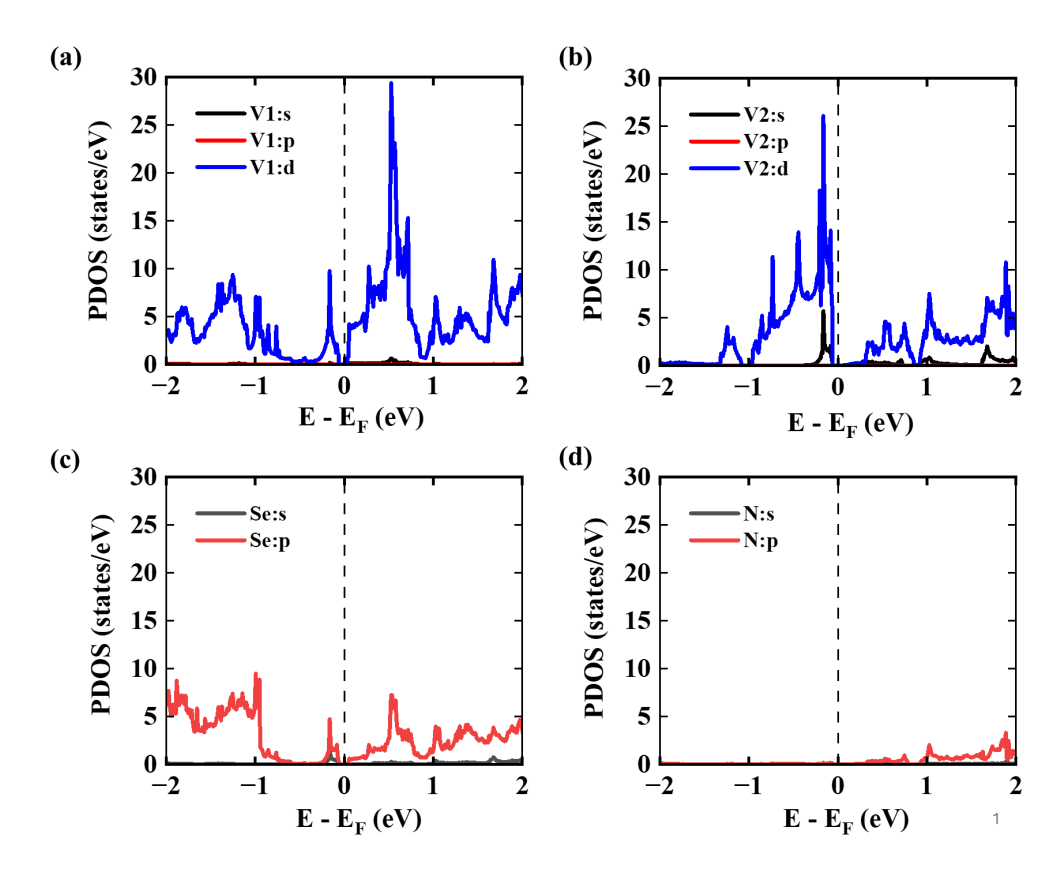


Figure 7: Orbital PDOS of VSe_2/VN (2×2×1 supercell). (a) Projection of s, p, d orbitals of V1 (V atom of VSe_2). (b) Projection of s, p, d orbitals of V2 (V atom of VN). (c) Projection of s, p orbitals of Se. (d) Projection of s, p orbitals of N.

total magnetization is saturated at 3.00 μ_B per unit cell, as illustrated in Fig. 9(c).

3.5 Effect of Biaxial Strain on Band Structure

Figs. 8(a–i) show the evolution of the band structure under biaxial strain. Under compressive strain and in the unstrained case (Figs. 8(a–e)), both spin channels retained a finite band gap, whereas under tensile strain (Figs. 8(f–i)), only the spin-down channel exhibited an increasing gap, while the spin-up gap collapsed. This behavior in VSe₂/VN enables enhanced spin selectivity near the Fermi level. A strain-controlled $|\Delta C_{KK'}|$ was also observed in both spin channels. For the spin-down channel, $|\Delta C_{KK'}|$ varied substantially with strain, whereas for the spin-up channel, $|\Delta C_{KK'}|$ remained nearly constant as the strain was increased from compressive to tensile.

We plotted these observations in Figs. 9(a) and (b). In Fig. 9(a), $|\Delta C_{KK'}|$ is shown with respect to strain for both spin channels. The spin-down $|\Delta C_{KK'}|$ exhibited a pronounced, non-monotonic response: it increased from 44.2 meV at -4% to a maximum of 72.5 meV at -3%, then gradually decreased through zero strain (61.3 meV) to a minimum of 42.9 meV at +3%, followed by a slight rebound to 44.1 meV at +4%. Overall, the spin-down splitting varied over a wide range (~ 30 meV, $\sim 50\%$ of the zero-strain value), indicating strong tunability by biaxial strain. In contrast, the spin-up $|\Delta C_{KK'}|$ remained comparatively small

and weakly strain-dependent: it increased from 8.4 meV at -4% to 23.4 meV at -2% and then saturated near ~ 20 meV for $-1\% \rightarrow +4\%$ (ending at 19.3 meV). These trends show that strain chiefly modulates the spin-down valley splitting, while the spin-up channel is relatively insensitive.

Fig. 9(b) summarizes the spin-resolved band gaps (in eV) versus biaxial strain. The spin-down gap increased monotonically from 0.13 eV at -4% to 0.99 eV at +4%, passing through 0.64 eV at zero strain. In contrast, the spin-up gap showed a non-monotonic trend: it rose under compression, peaking at 0.35 eV at -2%, then decreased to 0.11 eV at 0% and collapsed to 0 for tensile strains $\geq +1\%$. Thus, tensile strain drives a spin-selective regime in which the spin-down channel remains semiconducting with an enlarging gap, whereas the spin-up channel becomes gapless, consistent with a half-metallic behavior under tension.

Fig. 9(c) lists the strain dependence of the total and absolute magnetizations (in $\mu_{\rm B}$ per unit cell). The total magnetization increased steadily from 2.83 $\mu_{\rm B}$ at -4% to 2.99 $\mu_{\rm B}$ at 0%, and then saturated at 3.00 $\mu_{\rm B}$ for tensile strains \geq +1%. In contrast, the absolute magnetization rose almost monotonically across the entire range, from 3.81 $\mu_{\rm B}$ at -4% to 4.93 $\mu_{\rm B}$ at +4%. This behavior is fully consistent with the previously discussed spin density of VSe₂/VN at various strains..

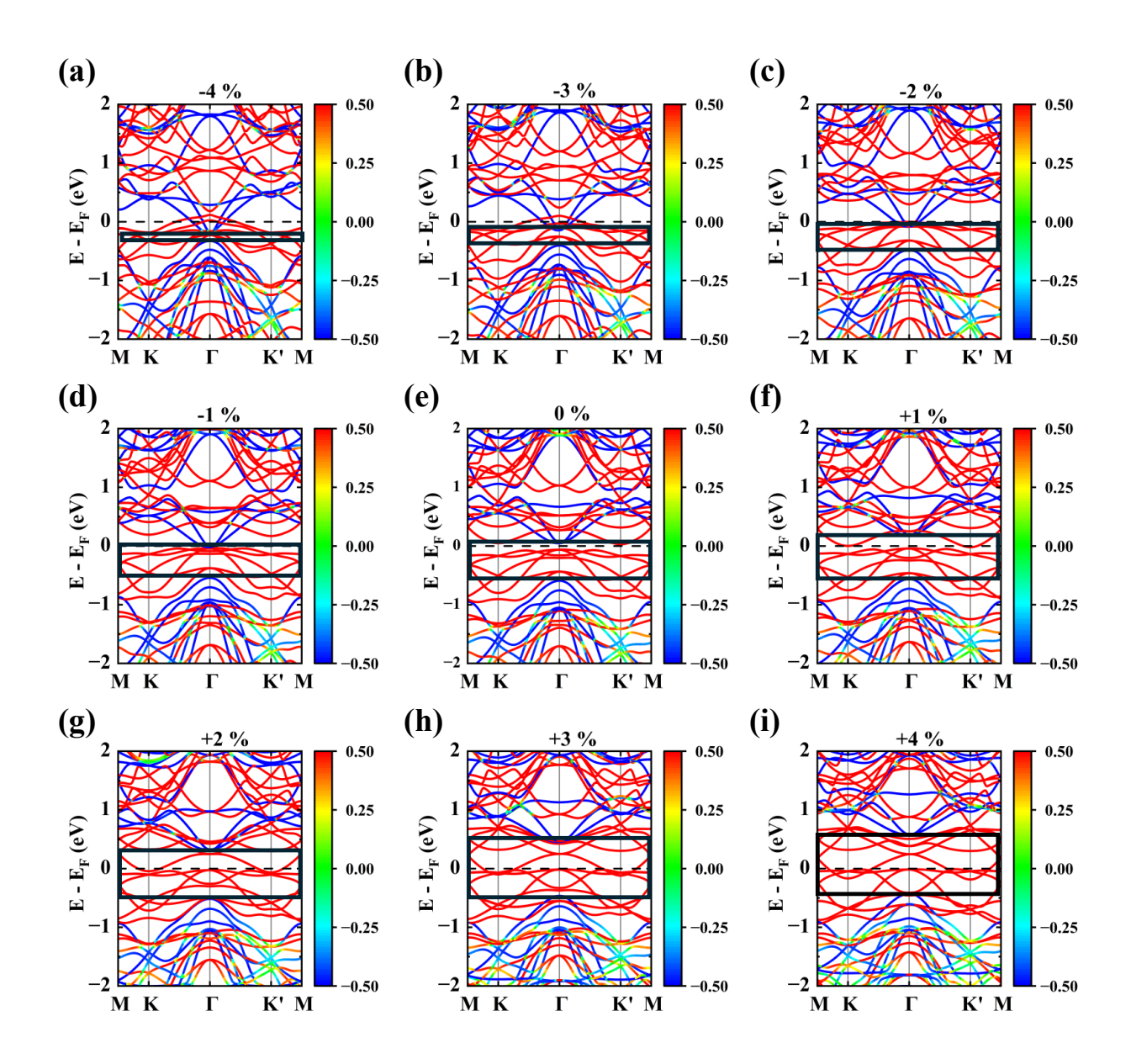


Figure 8: Effect of biaxial strain on band structure: (a) -4%, (b) -3%, (c) -2%, (d) -1%, (e) 0%, (f) +1%, (g) +2%, (h) +3% and (i) +4%. Panels (a)–(d) represent compressive strain, while (e)–(i) show tensile strain. The rectangular box shows the increasing gap of the spin-down channel.

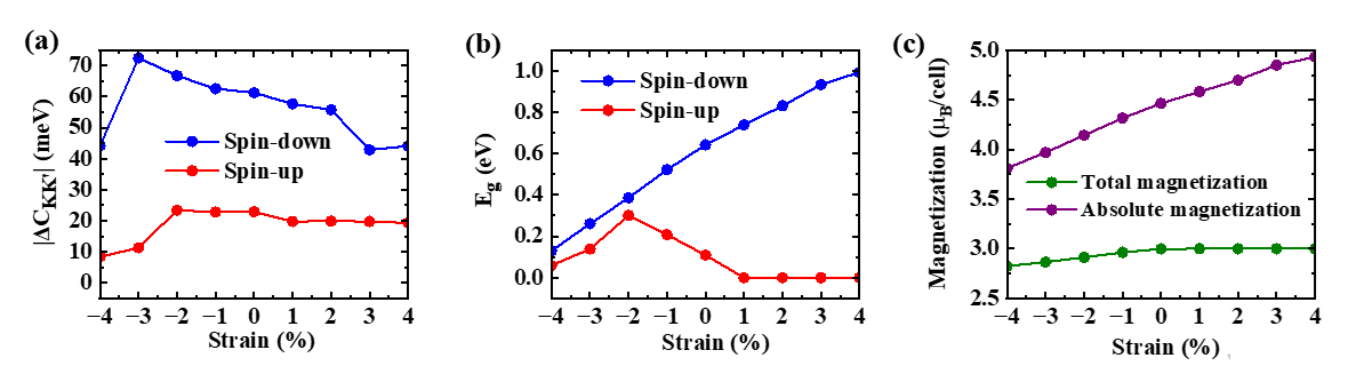


Figure 9: (a) Magnitude of conduction band valley splitting, $|\Delta C_{KK'}|$, (b) bandgap, E_g of spin-down and spin-up channels, and (c) total and absolute magnetization with respect to various strains (both compressive and tensile) of VSe₂/VN heterostructure.

3.6 Berry Curvature and Anomalous Hall Effect

In condensed matter physics, Berry curvature acts as an effective magnetic field in momentum space for Bloch electrons when TRS or SIS is broken [56, 57]. The Berry curvature in the conduction band is given by [9],

$$\Omega_{c,s}(k) = -\tau_z \frac{2 a^2 t^2 \Delta}{\left(4 a^2 t^2 k^2 + \Delta^2\right)^{3/2}}$$
 (13)

Here, k is the crystal momentum measured from K or K', Δ is the bandgap at k, t is the hopping integral, a is the lattice constant, and $\tau_z = \pm 1$ is the valley index.

In the presence of an in-plane electric field, E, this Berry curvature directly drives transverse anomalous velocities according to

$$v_{\text{transverse}} = \frac{e}{\hbar} E \times \Omega(k)$$
 (14)

Due to broken TRS or SIS, the Berry curvature will be opposite and unequal at K and K' valleys. As a result, $v_{transverse}$ will be opposite and asymmetric at these valleys, resulting in a generation of voltage known as anomalous Hall voltage.

The anomalous Hall conductivity or AHC was obtained by integrating the Berry curvature over all occupied states in the Brillouin zone,

$$\sigma_{xy} = \frac{e^2}{\hbar} \int_{BZ} \frac{d^2k}{(2\pi)^2} f(k) \Omega(k)$$
 (15)

where f(k) is the Fermi–Dirac distribution function. VSe_2/VN heterostructure has both broken TRS and SIS. As illustrated in Fig. 10(a), a non-zero net Berry curvature is observed at K and K'. At the K valley, $-\Omega_z$ was -9.05 Å 2 , whereas at the K' valley it was 6.24 Å 2 , confirming a finite net Berry curvature. Smaller features appeared around Γ , and between K and Γ , with several zero crossings indicated by the dashed baseline. A two-dimensional contour map of the Berry curvature over the hexagonal Brillouin zone is shown in Fig. 10(b). The alternating blue and red hot spots at K and K' provide direct evidence for the presence of the anomalous Hall effect (AHE) in this heterostructure.

In Fig. 10(c), the AHC denoted by σ_{xy} , is shown. For the spin-up channel, the maximum σ_{xy} within the K/K' energy window was 568.33 S/cm, whereas for the spin-down channel it was 216.45 S/cm. Because the spin-up bands were closer to E_F , the AHC was dominated by the spin-up contribution. This large value of AHC underscores the potential for realizing robust AHE in VSe₂/VN.

3.7 Proposed Tunable Spin-Filter and Valleytronic Device

To evaluate the spin-filtering efficiency of VSe₂/VN, we followed the low-bias Wentzel-Kramers-Brillouin (WKB) description of spin-dependent tunneling as mentioned in

previous literatures [58, 59]. The spin-resolved current densities scale exponentially with the decay constants inside the barrier,

$$J_{\uparrow,\downarrow} \propto \exp\left[-2\kappa_{\uparrow,\downarrow}d\right], \qquad \kappa_{\uparrow,\downarrow} = \frac{\sqrt{2\,m^*\,\Phi_{\uparrow,\downarrow}}}{\hbar}$$
 (16)

where the spin-dependent barrier heights are written as symmetric deviations about their mean,

$$\Phi_{\uparrow,\downarrow} = \bar{\Phi} \mp \frac{\Delta\Phi}{2}, \qquad \Delta\Phi = \Phi_{\downarrow} - \Phi_{\uparrow}$$
(17)

The spin-filtering efficiency is then defined as

$$P = \frac{J_{\uparrow} - J_{\downarrow}}{J_{\uparrow} + J_{\downarrow}} \tag{18}$$

Here, $J_{\uparrow,\downarrow}$ denotes spin-up and spin-down tunneling current densities, d is the barrier thickness, m^* is the electron effective mass and $\Phi_{\uparrow,\downarrow}$ is the spin-dependent barrier heights.

Fig. 11(a) demonstrates spin-filter tunability of VSe₂/VN under biaxial tensile strain. Biaxial strain can be applied using wafer-bending method, as described in the literature [60]. At 0% and +4% strain, the gaps were 0.64 and 0.99 eV, respectively; this gap served as the tunneling barrier for the spin-down channel. Using the spin-filtering efficiency expression, we obtained P = 75.4% for the unstrained case and P = 82.5% at +4% tensile strain, indicating a clear improvement. We focused on +4% because it yielded a higher DOS near E_E than in the unstrained case (Figs. S5(a) and (b)), with an \sim 8.4 times enhancement of spin-up carriers (Section S6 of Supplementary Material). Thus, tensile strain simultaneously increases both efficiency and spin-up carrier concentration. The trade-off is a reduction of the Curie temperature from 284.04 K to 183.9 K, implying that cryogenic operation would be required for robust ferromagnetism at +4% strain.

A valleytronic transistor based on VSe $_2$ /VN can be realized with source, drain, a back gate, and lateral probes A and B. An analogous valleytronic transistor was demonstrated for MoS $_2$ on SiO $_2$ /Si in the study [61]. Figs. 11(b) and 11(c) show the top and side views of the proposed device. When a drain–source bias V $_{DS}$ will be applied, electrons will flow along the channel; the opposite Berry curvatures at K and K' will deflect carriers to opposite edges, producing an anomalous Hall voltage V $_{H}$ between probes A and B. The back-gate voltage V $_{G}$ will tune the Fermi level E_{F} and thereby modulate V $_{H}$.

4 Comparative Analysis

In Table 6, VSe₂/VN shows a balanced and superior performance across all four metrics: Curie temperature T_C , spin-filtering efficiency P, conduction band valley splitting $\Delta C_{KK'}$, and maximum anomalous Hall conductivity $|\sigma_{xy}|$ evaluated between K and K' energy. Specifically, VSe₂/VN attained $T_C = 284.04$ K with P = 75.4%, exceeding $W_{0.25}V_{0.75}Se_2$ (59.57 K, 42%) [19], EuO (69.3 K, 29%) [6] and EuS (16.6 K, 86%) [6] by providing near-ambient T_C

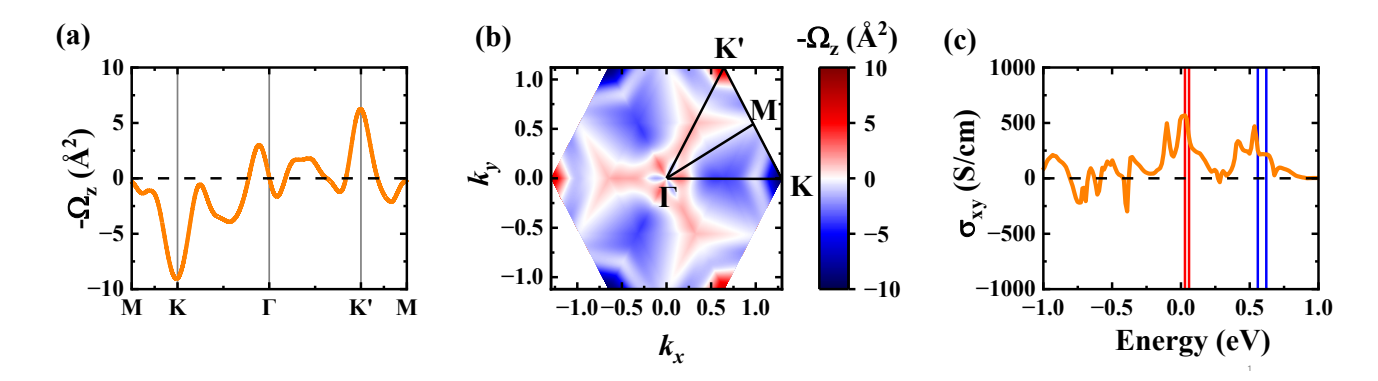


Figure 10: (a) Berry curvature, $-\Omega_z$ (Ų) along the high-symmetry path $M \to K \to \Gamma \to K' \to M$, showing valley-contrasting behavior at K and K' points. (b) A 2D contour plot of Berry curvature, $-\Omega_z$ (Ų) showing opposite valley index at alternating K and K' points over the whole hexagonal Brillouin zone (high-symmetry path is marked in the figure). (c) Anomalous Hall conductivity, σ_{xy} of VSe₂/VN (red and blue lines indicate the K and K' valleys' energy range of the spin-up and spin-down band structures' CBM, respectively).

 Table 6

 Comparative study of 2D systems exhibiting spin-filtering, valley properties and anomalous Hall effect

Structure	Curie Temperature, $T_{\rm C}$ (K)	Spin-filtering efficiency, P (%)	$\begin{array}{c} \text{Conduction} \\ \text{band valley} \\ \text{splitting, } \Delta C_{KK'} \\ \text{(meV)} \end{array}$	$\begin{array}{c} \text{Maximum anomalous Hall} \\ \text{conductivity, } \sigma_{xy} \text{ (S/cm) between} \\ \text{K and K' energy} \end{array}$	Reference
$W_{0.25}V_{0.75}Se_2$	59.57	42	_	_	[19]
EuO	69.3	29	_	_	[6]
EuS	16.6	86	_	_	[6]
VSe_2/VN	284.04	75.4	22.9	568.33	This study
$NbSe_2$	176.25	_	18.6	~ 59	[25]
V-doped AgBiP ₂ S ₆	_	_	26.8	~ 120	[62]
GdI_2	_	-	149	~ 13	[63]

while maintaining high P. For valley properties, VSe₂/VN exhibited $\Delta C_{KK'}=22.9$ meV, comparable to V-doped AgBiP₂S₆ (26.8 meV) [62] and NbSe₂ (18.6 meV) [25] and below GdI₂ (149 meV) [63]. The AHC of VSe₂/VN outperformed the other systems. It reached $|\sigma_{xy}|=568.33$ S/cm, larger in magnitude than NbSe₂ (~ 59 S/cm), V-doped AgBiP₂S₆ (~ 120 S/cm) and GdI₂ (~ 13 S/cm). Entries for W_{0.25}V_{0.75}Se₂, EuO, and EuS remain absent for $\Delta C_{KK'}$ and σ_{xy} , indicating no reported valley-resolved Hall data. Taken together, these comparisons show that only this study (VSe₂/VN) simultaneously demonstrated robust spin filtering and clear valley-related phenomena; namely a finite $\Delta C_{KK'}$ in the conduction band together with a large σ_{xy} between K and K' which constitutes the central novelty of our work.

Conclusion

In this paper, we explored the VSe₂/VN van der Waals heterostructure and established that the AA-stacked configuration (stacking 2) was the most stable, exhibiting a

formation energy of -0.95 eV per unit cell and an inplane lattice parameter of 3.328 Å. We further found that charge transferred from the VN layer to the VSe2 layer upon forming the heterostructure, consistent with the work functions of VSe₂ (5.47 eV), VN (3.81 eV), and the combined system (4.53 eV), which aligned at the interface. The optimized structure yielded Se-V-Se and V-N-V/N-V-N bond angles of 79.29° and 120°, respectively, confirming minimal distortion of the constituent layers. Electrically and magnetically, the heterostructure displayed key ferrovalley features with a sizable and strain-tunable conduction band valley splitting in both spin channels ($\Delta C_{KK'} = 22.9 \text{ meV}$ for spin-up and $\Delta C_{KK'} = 61.3 \text{ meV}$ for spin-down) including total magnetization of 3.00 $\mu_{\rm B}$ per unit cell, out-ofplane easy axis at unstrained and tensile strain cases, and strong Berry-curvature-driven transport, culminating in a maximum anomalous Hall conductivity of 568.33 (S/cm). Importantly, the heterostructure had a Curie temperature of 284.04 K and a spin-filtering efficiency of 75.4% in the unstrained case and tensile strain-tunable up to 82.5% with a sacrifice in Curie temperature (183.9 K), demonstrating concurrent prospects for valleytronic and spintronic device

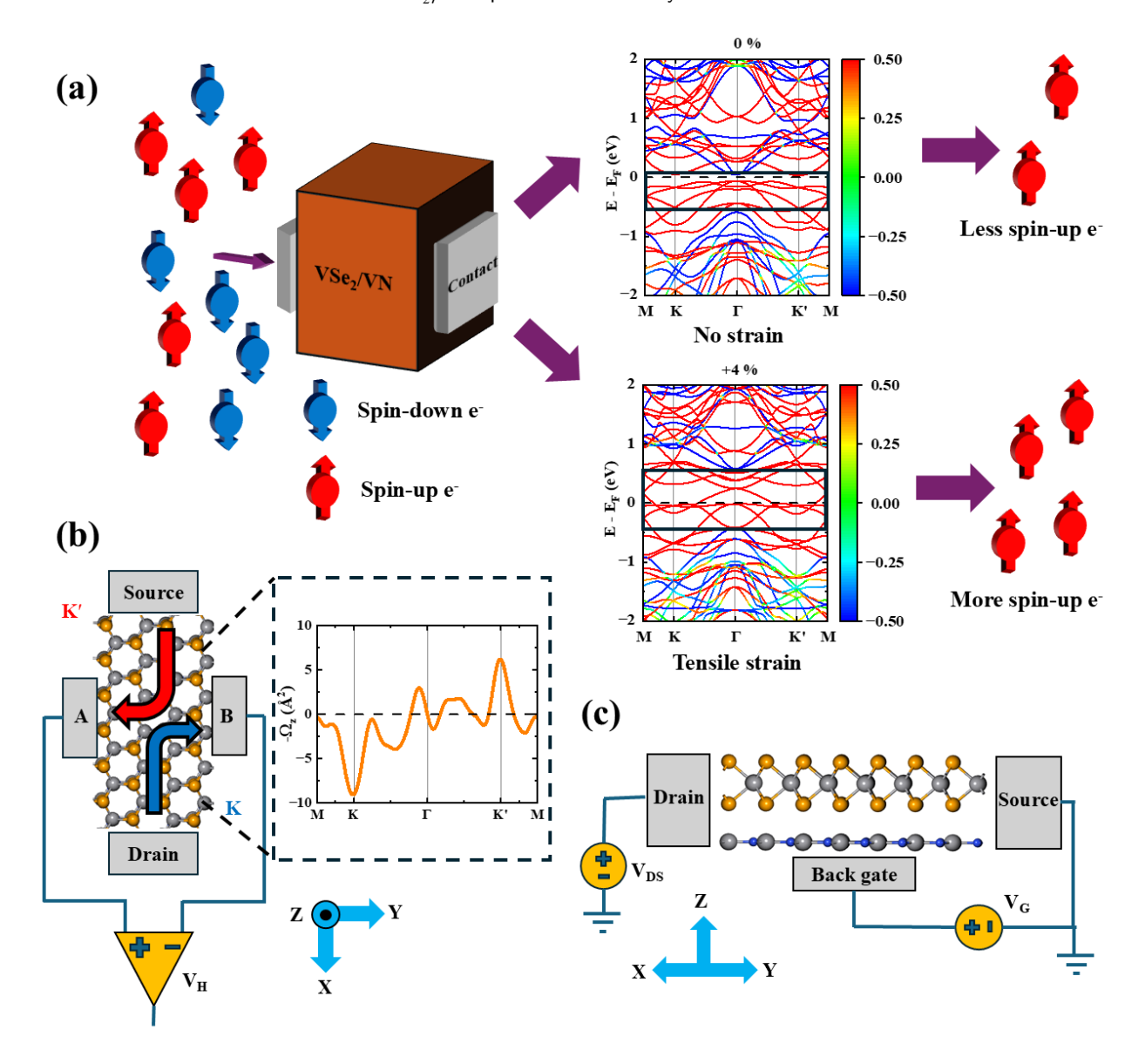


Figure 11: (a) Tunability of spin-filter. Tensile strain favors high spin-filtering efficiency along with high spin-up electron concentration. (b) Top and (c) side view of the proposed valleytronic device with drain, source, back gate and probes A and B. Anomalous Hall voltage, $V_{\rm H}$ will appear between A and B.

concepts in a single material platform. These results revealed that VSe₂/VN combined robust thermodynamic stability with interfacial charge redistribution and spin–valley functionality, positioning it as a promising candidate for next-generation spin-filtering and valleytronic applications.

CRediT authorship contribution statement

Vivek Chowdhury: Conceptualization, Methodology, Visualization, Software, Investigation, Writing – original draft. **Ahmed Zubair:** Conceptualization, Methodology, Visualization, Resources, Funding acquisition, Writing – original draft, Writing – review & editing, Supervision.

Declaration of Competing Interest

The authors declare that they have no known competing financial interests or personal relationships that could have appeared to influence the work reported in this paper.

Data Availability Statement

The data supporting the findings presented in this paper are not currently available to the public, but they may be obtained from the authors upon reasonable request.

Acknowledgements

V.C. and A.Z. thank the Bangladesh University of Engineering and Technology (BUET) and the Bangladesh Research and Education Network (BdREN) for providing computational facilities and technical support. A.Z. and V.C. further thank the Research and Innovation Centre for Science and Engineering (RISE), BUET, for financial support through the Internal Research Grant (Project ID: 2023-02-022).

Supplementary Material

See Supplementary Material at https://....

References

- Robert H Dennard, Fritz H Gaensslen, Hwa-Nien Yu, V Leo Rideout, Ernest Bassous, and Andre R LeBlanc. Design of ion-implanted mosfet's with very small physical dimensions. *IEEE Journal of solid-state circuits*, 9(5):256–268, 2003.
- [2] Mark Horowitz, Elad Alon, Dinesh Patil, Samuel Naffziger, Rajesh Kumar, and Kerry Bernstein. Scaling, power, and the future of cmos. In *IEEE International Electron Devices Meeting*, 2005. *IEDM Technical Digest.*, pages 7–pp. IEEE, 2005.
- [3] Atsufumi Hirohata, Keisuke Yamada, Yoshinobu Nakatani, Ioan-Lucian Prejbeanu, Bernard Diény, Philipp Pirro, and Burkard Hillebrands. Review on spintronics: Principles and device applications. *Journal of Magnetism and Magnetic Materials*, 509:166711, 2020.
- [4] Igor Žutić, Jaroslav Fabian, and S Das Sarma. Spintronics: Fundamentals and applications. Reviews of modern physics, 76(2):323, 2004
- [5] WH Butler, X-G Zhang, TC Schulthess, and JM MacLaren. Spin-dependent tunneling conductance of Fe | MgO | Fe sandwiches. Physical Review B, 63(5):054416, 2001.
- [6] Koichiro Inomata, Naomichi Ikeda, Nobuki Tezuka, Ryogo Goto, Satoshi Sugimoto, Marek Wojcik, and Eva Jedryka. Highly spinpolarized materials and devices for spintronics. Science and Technology of Advanced Materials, 9(1):014101, 2008.
- [7] Yufang Xie, Su-Yun Zhang, Yin Yin, Naihang Zheng, Anwar Ali, Muhammad Younis, Shuangchen Ruan, and Yu-Jia Zeng. Emerging ferromagnetic materials for electrical spin injection: towards semiconductor spintronics. npj Spintronics, 3(1):10, 2025.
- [8] Tiancheng Song, Xinghan Cai, Matisse Wei-Yuan Tu, Xiaoou Zhang, Bevin Huang, Nathan P Wilson, Kyle L Seyler, Lin Zhu, Takashi Taniguchi, Kenji Watanabe, et al. Giant tunneling magnetoresistance in spin-filter van der waals heterostructures. *Science*, 360(6394):1214–1218, 2018.
- [9] John R Schaibley, Hongyi Yu, Genevieve Clark, Pasqual Rivera, Jason S Ross, Kyle L Seyler, Wang Yao, and Xiaodong Xu. Valleytronics in 2d materials. *Nature Reviews Materials*, 1(11):1–15, 2016.
- [10] Christoph E Nebel. Electrons dance in diamond. *Nature materials*, 12(8):690–691, 2013.
- [11] Sintayehu Mekonnen and Pooran Singh. Dopant introduced valley polarization, spin, and valley hall conductivity in doped monolayer mos2. Advances in Condensed Matter Physics, 2018(1):1303816, 2018.
- [12] Zhiya Zhang, Xiaojuan Ni, Huaqing Huang, Lin Hu, and Feng Liu. Valley splitting in the van der waals heterostructure WSe₂/CrI₃: The role of atom superposition. *Physical Review B*, 99(11):115441, 2019.
- [13] Baoxing Zhai, Juan Du, Chenhai Shen, Tianxing Wang, Yuting Peng, Qiming Zhang, and Congxin Xia. Spin-dependent dirac electrons and valley polarization in the ferromagnetic stanene/CrI₃ van der waals heterostructure. *Physical Review B*, 100(19):195307, 2019.

- [14] Ding Zhong, Kyle L Seyler, Xiayu Linpeng, Nathan P Wilson, Takashi Taniguchi, Kenji Watanabe, Michael A McGuire, Kai-Mei C Fu, Di Xiao, Wang Yao, et al. Layer-resolved magnetic proximity effect in van der waals heterostructures. *Nature nanotechnology*, 15(3):187– 191, 2020.
- [15] Kin Fai Mak, Jie Shan, and Daniel C Ralph. Probing and controlling magnetic states in 2d layered magnetic materials. *Nature Reviews Physics*, 1(11):646–661, 2019.
- [16] João CG Henriques, Gonçalo Catarina, António T Costa, Joaquín Fernández-Rossier, and Nuno MR Peres. Excitonic magneto-optical kerr effect in two-dimensional transition metal dichalcogenides induced by spin proximity. *Physical Review B*, 101(4):045408, 2020.
- [17] Gonçalo Catarina, Nuno MR Peres, and Joaquín Fernández-Rossier. Magneto-optical kerr effect in spin split two-dimensional massive dirac materials. 2D Materials, 7(2):025011, 2020.
- [18] Kai Ren, MingLei Sun, Yi Luo, SaKe Wang, Jin Yu, and WenCheng Tang. First-principle study of electronic and optical properties of two-dimensional materials-based heterostructures based on transition metal dichalcogenides and boron phosphide. *Applied Surface Science*, 476:70–75, 2019.
- [19] Khondker Shihabul Hoque and Ahmed Zubair. First-principles study of induced magnetism in tungsten vanadium selenide alloys for spintronic applications. ACS Omega, 7(41):36184–36194, 2022.
- [20] X.W. Zhao, Y. Li, R.D. Liang, G.C. Hu, X.B. Yuan, and J.F. Ren. Enhanced valley polarization at valence/conduction band in transition-metal-doped WTe₂ under strain force. *Applied Surface Science*, 504:144367, 2020.
- [21] Khaled Mahmud, Taki Yashir, and Ahmed Zubair. First-principles calculations on monolayer WX₂ (X = S, Se) as an effective drug delivery carrier for anti-tuberculosis drugs. *Nanoscale Advances*, 6:2447–2458, 2024.
- [22] Hope Bretscher, Zhaojun Li, James Xiao, Diana Yuan Qiu, Sivan Refaely-Abramson, Jack A. Alexander-Webber, Arelo Tanoh, Ye Fan, Géraud Delport, Cyan A. Williams, Samuel D. Stranks, Stephan Hofmann, Jeffrey B. Neaton, Steven G. Louie, and Akshay Rao. Rational passivation of sulfur vacancy defects in two-dimensional transition metal dichalcogenides. ACS Nano, 15(5):8780–8789, 2021. PMID: 33983711
- [23] Di Xiao, Gui-Bin Liu, Wanxiang Feng, Xiaodong Xu, and Wang Yao. Coupled spin and valley physics in monolayers of MoS₂ and other group-vi dichalcogenides. *Physical review letters*, 108(19):196802, 2012.
- [24] Wang Yao, Di Xiao, and Qian Niu. Valley-dependent optoelectronics from inversion symmetry breaking. *Physical Review B—Condensed Matter and Materials Physics*, 77(23):235406, 2008.
- [25] Samiul Islam, Sharif Mohammad Mominuzzaman, and Ahmed Zubair. Tunable valley polarization and anomalous hall effect in ferrovalley NbX₂ and TaX₂ (X = S, Se, Te): A first-principles study. Applied Surface Science, xx:165094, 2025.
- [26] Xiaofei Bian, Shuang Lian, Bin Fu, and Yukai An. Tunable spin-valley splitting and magnetic anisotropy of two-dimensional 2H-VS₂/h-VN heterostructure. *Journal of Magnetism and Magnetic Materials*, 546:168867, 2022.
- [27] Xiao Liang, Longjiang Deng, Fei Huang, Tingting Tang, Chuangtang Wang, Yupeng Zhu, Jun Qin, Yan Zhang, Bo Peng, and Lei Bi. The magnetic proximity effect and electrical field tunable valley degeneracy in MoS₂/EuS van der waals heterojunctions. *Nanoscale*, 9(27):9502–9509, 2017.
- [28] Qingyun Zhang, Shengyuan A Yang, Wenbo Mi, Yingchun Cheng, and Udo Schwingenschlögl. Large spin-valley polarization in monolayer MoTe₂ on top of euo (111). Advanced Materials, 28(5):959–966, 2016
- [29] Chuan Zhao, Tenzin Norden, Peiyao Zhang, Puqin Zhao, Yingchun Cheng, Fan Sun, James P Parry, Payam Taheri, Jieqiong Wang, Yihang Yang, et al. Enhanced valley splitting in monolayer WSe₂ due to magnetic exchange field. *Nature nanotechnology*, 12(8):757–762, 2017.

- [30] Kyle L Seyler, Ding Zhong, Bevin Huang, Xiayu Linpeng, Nathan P Wilson, Takashi Taniguchi, Kenji Watanabe, Wang Yao, Di Xiao, Michael A McGuire, et al. Valley manipulation by optically tuning the magnetic proximity effect in WSe₂/CrI₃ heterostructures. *Nano letters*, 18(6):3823–3828, 2018.
- [31] Congming Ke, Yaping Wu, Weihuang Yang, Zhiming Wu, Chunmiao Zhang, Xu Li, and Junyong Kang. Large and controllable spin-valley splitting in two-dimensional WS₂/h-VN. *Physical Review B*, 100:195435, Nov 2019.
- [32] Xiao Liang, Yiqun Liu, Tianjun Zhong, Ting Yang, Jie Li, Li Luo, Gao Dong, Yanhong Chen, Xuelian Luo, Tingting Tang, et al. Mechanisms of manipulating valley splitting in MoTe₂/MnS₂ van der waals heterostructure by electric field and strains. *RSC advances*, 14(15):10209–10218, 2024.
- [33] Imran Khan, Javed Ahmad, Muhammad Ehsan Mazhar, and Jisang Hong. Strain tuning of the curie temperature and valley polarization in two dimensional ferromagnetic WSe₂/CrSnSe₃ heterostructure. *Nanotechnology*, 32(37):375708, 2021.
- [34] Bing-Jie Wang, Yu-Yun Sun, Ju Chen, Weiwei Ju, Yi-Peng An, and Shi-Jing Gong. Valley splitting in the antiferromagnetic heterostructure MnPSe₃/WSe₂. J. Mater. Chem. C, 9:3562–3568, 2021.
- [35] Zhida Zheng, Xiaocha Wang, and Wenbo Mi. Strain and electric-field tunable valley states in 2d van der waals MoTe₂/WTe₂ heterostructures. *Journal of Physics: Condensed Matter*, 28(50):505003, 2016.
- [36] Huei-Ru Fuh, Ching-Ray Chang, Yin-Kuo Wang, Richard FL Evans, Roy W Chantrell, and Horng-Tay Jeng. Newtype single-layer magnetic semiconductor in transition-metal dichalcogenides VX₂ (X= S, Se and Te). Scientific reports, 6(1):32625, 2016.
- [37] Jia Li, Bei Zhao, Peng Chen, Ruixia Wu, Bo Li, Qinglin Xia, Guanghua Guo, Jun Luo, Ketao Zang, Zhengwei Zhang, et al. Synthesis of ultrathin metallic MTe₂ (M= V, Nb, Ta) single-crystalline nanoplates. Advanced Materials, 30(36):1801043, 2018.
- [38] Chen Wang and Yukai An. Effects of strain and stacking patterns on the electronic structure, valley polarization and magnetocrystalline anisotropy of layered VTe₂. Applied Surface Science, 538:148098, 2021
- [39] Vinayak Musle, Abhishek Kumar, and Sudhanshu Choudhary. Temperature dependent spin transport investigations in single layer VTe₂. *Journal of Alloys and Compounds*, 770:345–349, 2019.
- [40] Shengnan Feng and Wenbo Mi. Strain and interlayer coupling tailored magnetic properties and valley splitting in layered ferrovalley 2H-VSe₂. Applied Surface Science, 458:191–197, 2018.
- [41] Manuel Bonilla, Sadhu Kolekar, Yujing Ma, Horacio Coy Diaz, Vijaysankar Kalappattil, Raja Das, Tatiana Eggers, Humberto R Gutierrez, Manh-Huong Phan, and Matthias Batzill. Strong roomtemperature ferromagnetism in VSe₂ monolayers on van der waals substrates. *Nature nanotechnology*, 13(4):289–293, 2018.
- [42] Georgy V Pushkarev, Vladimir G Mazurenko, Vladimir V Mazurenko, and Danil W Boukhvalov. Structural phase transitions in VSe₂: Energetics, electronic structure and magnetism. *Physical Chemistry Chemical Physics*, 21(40):22647–22653, 2019.
- [43] Artem V Kuklin, Svetlana A Shostak, and Alexander A Kuzubov. Two-dimensional lattices of vn: emergence of ferromagnetism and half-metallicity on nanoscale. *The Journal of Physical Chemistry Letters*, 9(6):1422–1428, 2018.
- [44] Paolo Giannozzi, Stefano Baroni, Nicola Bonini, Matteo Calandra, Roberto Car, Carlo Cavazzoni, Davide Ceresoli, Guido L Chiarotti, Matteo Cococcioni, Ismaila Dabo, et al. Quantum espresso: a modular and open-source software project for quantum simulations of materials. *Journal of physics: Condensed matter*, 21(39):395502, 2009.
- [45] Atsushi Togo, Laurent Chaput, Terumasa Tadano, and Isao Tanaka. Implementation strategies in phonopy and phono3py. *Journal of Physics: Condensed Matter*, 35(35):353001, 2023.
- [46] Graeme Henkelman, Andri Arnaldsson, and Hannes Jónsson. A fast and robust algorithm for bader decomposition of charge density. *Computational Materials Science*, 36(3):354–360, 2006.
- [47] Giovanni Pizzi, Valerio Vitale, Ryotaro Arita, Stefan Blügel, Frank Freimuth, Guillaume Géranton, Marco Gibertini, Dominik

- Gresch, Charles Johnson, Takashi Koretsune, Julen Ibañez-Azpiroz, Hyungjun Lee, Jae-Mo Lihm, Daniel Marchand, Antimo Marrazzo, Yuriy Mokrousov, Jamal I Mustafa, Yoshiro Nohara, Yusuke Nomura, Lorenzo Paulatto, Samuel Poncé, Thomas Ponweiser, Junfeng Qiao, Florian Thöle, Stepan S Tsirkin, Małgorzata Wierzbowska, Nicola Marzari, David Vanderbilt, Ivo Souza, Arash A Mostofi, and Jonathan R Yates. Wannier90 as a community code: new features and applications. *Journal of Physics: Condensed Matter*, 32(16):165902, jan 2020.
- [48] AHM Wasey, Soubhik Chakrabarty, and GP Das. Quantum size effects in layered VX₂ (X= S, Se) materials: Manifestation of metal to semimetal or semiconductor transition. *Journal of Applied Physics*, 117(6), 2015
- [49] Guiyuan Hua, Xuming Wu, Xujin Ge, Tianhang Zhou, and Zhibin Shao. First-principles study on the high spin-polarized ferromagnetic semiconductor of vanadium-nitride monolayer and its heterostructures. *Molecules*, 30(10):2156, 2025.
- [50] Zhong-Liu Liu, Xu Wu, Yan Shao, Jing Qi, Yun Cao, Li Huang, Chen Liu, Jia-Ou Wang, Qi Zheng, Zhi-Li Zhu, et al. Epitaxially grown monolayer VSe₂: an air-stable magnetic two-dimensional material with low work function at edges. *Science bulletin*, 63(7):419–425, 2018.
- [51] Jiawen You, Jie Pan, Shun-Li Shang, Xiang Xu, Zhenjing Liu, Jingwei Li, Hongwei Liu, Ting Kang, Mengyang Xu, Shaobo Li, et al. Salt-assisted selective growth of h-phase monolayer VSe₂ with apparent hole transport behavior. *Nano letters*, 22(24):10167–10175, 2022.
- [52] Bogdan Warcholinski, Adam Gilewicz, Alexandr S Kuprin, Galina N Tolmachova, Elena N Reshetnyak, Ilya O Klimenko, Igor V Kolodiy, Ruslan L Vasilenko, and Maria Tarnowska. Mechanical properties of von coatings synthesized by cathodic arc evaporation. *Materials*, 17(2):419, 2024.
- [53] Diancheng Chen, Xueling Lei, Yanan Wang, Shuying Zhong, Gang Liu, Bo Xu, and Chuying Ouyang. Tunable electronic structures in bp/mosse van der waals heterostructures by external electric field and strain. Applied Surface Science, 497:143809, 2019.
- [54] Jibo Liu, Yuheng Jin, Bocheng Lei, Xucai Zhao, Yineng Huang, Lili Zhang, and Youliang Zhu. Studies on electronic structure and optical properties of MoS₂/X (X= WSe₂, MoSe₂, AlN, and ZnO) heterojunction by first principles. *Catalysts*, 14(10):678, 2024.
- [55] I Turek, J Kudrnovský, G Bihlmayer, and S Blügel. Ab initio theory of exchange interactions and the curie temperature of bulk gd. *Journal* of Physics: Condensed Matter, 15(17):2771, apr 2003.
- [56] Di Xiao, Ming-Che Chang, and Qian Niu. Berry phase effects on electronic properties. *Reviews of Modern Physics*, 82:1959–2007, Jul 2010
- [57] Ming-Che Chang and Qian Niu. Berry phase, hyperorbits, and the hofstadter spectrum. *Physical Review Letters*, 75:1348–1351, Aug 1995.
- [58] John G Simmons. Generalized formula for the electric tunnel effect between similar electrodes separated by a thin insulating film. *Journal* of applied physics, 34(6):1793–1803, 1963.
- [59] P. M. Tedrow and R. Meservey. Spin-dependent tunneling into ferromagnetic nickel. *Physical Review Letters*, 26:192–195, Jan 1971.
- [60] Ankit Kumar, Lin Xu, Arnab Pal, Kunjesh Agashiwala, Kamyar Parto, Wei Cao, and Kaustav Banerjee. Strain engineering in 2d fets: Physics, status, and prospects. *Journal of Applied Physics*, 136(9), 2024.
- [61] Lingfei Li, Lei Shao, Xiaowei Liu, Anyuan Gao, Hao Wang, Binjie Zheng, Guozhi Hou, Khurram Shehzad, Linwei Yu, Feng Miao, et al. Room-temperature valleytronic transistor. *Nature nanotechnology*, 15(9):743–749, 2020.
- [62] Dongxue Zhang and Baozeng Zhou. Conduction band-edge valley splitting in two-dimensional ferroelectric AgBiP₂S₆ by magnetic doping: towards electron valley-polarized transport. *RSC Advances*, 12:13765–13773, 2022.
- [63] Hai-Xia Cheng, Jun Zhou, Wei Ji, Yan-Ning Zhang, and Yuan-Ping Feng. Two-dimensional intrinsic ferrovalley GdI₂ with large valley polarization. *Physical Review B*, 103(12):125121, 2021.